



# Temperature and cloud condensation nuclei (CCN) sensitivity of orographic precipitation enhanced by a mixed-phase seeder–feeder mechanism: a case study for the 2015 Cumbria flood

Julia Thomas, Andrew Barrett, and Corinna Hoose

Institute of Meteorology and Climate Research, Department Troposphere Research (IMK-TRO),  
Karlsruhe Institute of Technology, Karlsruhe, Germany

**Correspondence:** Julia Thomas (julia.thomas@partner.kit.edu) and Corinna Hoose (corinna.hoose@kit.edu)

Received: 2 August 2022 – Discussion started: 23 August 2022

Revised: 1 December 2022 – Accepted: 7 January 2023 – Published: 8 February 2023

**Abstract.** The formation of orographic precipitation in mixed-phase clouds depends on a complex interplay of processes. This article investigates the microphysical response of orographic precipitation to perturbations of temperature and cloud condensation nuclei (CCN) concentration. A case study for the 2015 Cumbria flood in northern England is performed with sensitivities using a realization of the “piggybacking” method implemented into a limited-area setup of the Icosahedral Nonhydrostatic (ICON) model. A 6 % K<sup>-1</sup> enhancement of precipitation results for the highest altitudes, caused by a “mixed-phase seeder–feeder mechanism”, i.e. the interplay of melting and accretion. Total 24 h precipitation is found to increase by only 2 % K<sup>-1</sup>, significantly less than the 7 % K<sup>-1</sup> increase in atmospheric water vapour. A rain budget analysis reveals that the negative temperature sensitivity of the condensation ratio and the increase in rain evaporation dampen the precipitation enhancement. Decreasing the CCN concentration speeds up the microphysical processing, which leads to an increase in total precipitation. At low CCN concentration the precipitation sensitivity to temperature is systematically smaller. It is shown that the CCN and temperature sensitivities are to a large extent independent (with a ±3 % relative error) and additive.

## 1 Introduction

Orographically enhanced severe precipitation events are impacted by the increased water vapour capacity of the atmosphere in a warming climate and the general trend of increasing frequencies of extreme precipitation events (Pörtner et al., 2022). A detailed understanding of cloud microphysical processes that cause orographic precipitation is crucial to assess flood risk in the vicinity of low mountain ranges (Houze, 2012), now and in the future.

The relationship that dictates the atmospheric water vapour content is the Clausius–Clapeyron (CC) equation for saturation vapour pressure of water  $e_{\text{sat}}$ . In the atmospheric temperature range of interest in this work,  $e_{\text{sat}}$  increases between 6.5 % K<sup>-1</sup> and 9 % K<sup>-1</sup>. As shown in Fig. 1, the rel-

ative increase is stronger for lower temperatures, i.e. higher up in the atmosphere. The value of  $d\log(e_{\text{sat}})/dT$  for a given temperature is referred to as CC scaling throughout the paper. To a first approximation, relative humidity is constant in a warmer climate, since enhanced evaporation balances the increased capacity of the atmosphere to hold water vapour (Held and Soden, 2006). In particular, this holds for the upstream conditions of coastal orographic precipitation (Payne et al., 2020). A naive assumption might be that total precipitation increases by the same rate as atmospheric water vapour, but climate models predict that the global precipitation increases more slowly with global mean temperature than CC scaling (Allen and Ingram, 2002). Deviations from this assumption can be due to changes in dynamics (Pfahl et al., 2017), in the rate of condensation (thermodynamic

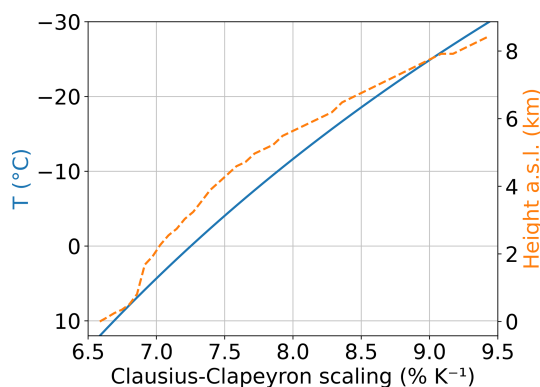


**Figure 1.** Clausius–Clapeyron scaling  $d\log(e_{\text{sat}})/dT$  as a function of temperature (solid blue) and as function of height above sea level (a.s.l.; dashed orange) in the study region for the simulated case.

effect) or in the microphysical processing of cloud water (O’Gorman, 2015). The thermodynamic effect originates in the temperature sensitivity of the CC scaling. Regionally, this leads to wet regions getting wetter and dry regions getting drier (Held and Soden, 2006). Locally, the relative increase in condensation is larger at high altitudes, according to the relative increase in water vapour. Siler and Roe (2014) showed that due to the temperature sensitivity of the moist adiabatic lapse rate, the increase in condensation is damped. It can lower the CC scaling by up to  $4\% \text{ K}^{-1}$  (Siler and Roe, 2014). Deviations from the CC scaling caused by cloud microphysics, which are characterized by the precipitation efficiency (PE), are the subject of this work.

An important microphysical effect that enhances orographic precipitation is the seeder–feeder effect (Bergeron, 1965). This mechanism requires at least two layers of cloud of which the upper one is precipitating. It has been observed in many studies all over the globe (within nimbostratus clouds as well as related to orographic clouds) (e.g. Bergeron, 1965; Stow et al., 1991; Kunz and Kottmeier, 2006a). The orographic cloud serves as a “feeder” cloud which is washed out by falling hydrometeors released from a “seeder” cloud aloft. The upper cloud can also be formed orographically. In most cases, however, it belongs to a layer of nimbostratus that usually forms along the warm front of a mid-latitude cyclone. One important feature of the mechanism is that the liquid water content (LWC) in the lower cloud is continuously replenished by the low-level moist flow. Growth processes involving both frozen and liquid hydrometeors (i.e. aggregation, riming, collision–coalescence) can contribute to the precipitation enhancement process.

Riming and collision–coalescence become less efficient for smaller cloud droplets and a narrower size distribution, as is the case in environments with higher cloud condensation nuclei (CCN) concentrations (Alizadeh-Choobari, 2018). This leads to a downwind shift in the surface rainfall distribution (Khain, 2009). If the raindrops are advected

into the evaporation region at the lee side of the mountain, the delayed onset of rainfall can lead to a decrease in total precipitation (Thompson and Eidhammer, 2014). In addition, smaller droplets can be lifted further up than larger droplets. This also favours advection into subsaturated regions. Meanwhile, droplets lifted above the freezing level can enhance graupel production by riming, which is a very efficient growth process. This can lead to complex responses of the distribution of precipitation. For example, Alizadeh-Choobari and Gharaylou (2017) found that for a case of convectively enhanced frontal precipitation over a mountainous region, light precipitation was reduced but moderate and strong precipitation intensified when the concentration of hygroscopic aerosols was increased. In general, the net effect highly depends on the synoptic conditions (e.g. whether convection is involved), on the model’s treatment of aerosols and on the mountain geometry (Kunz and Kottmeier, 2006a).

For the British Isles and mainland Europe, mid-latitude cyclones are the main drivers of wintertime precipitation (Douglas and Glasspoole, 1947). The seeder–feeder mechanism enhances orographic precipitation along coastal mountain ranges such as the British west coast (e.g. Browning et al., 1975; Smith et al., 2015) and can cause extreme orographic precipitation events such as the Cumbria flood in December 2015. Similar orographic precipitation events, e.g. at the Norwegian west coast (Sandvik et al., 2018), over the Oregon Cascade Range (Garvert et al., 2007) and over the southern Andes (Smith and Evans, 2007) as well as over the German Black Forest mountains (Kunz and Kottmeier, 2006b), have been investigated in previous works.

At the British west coast, moist air moving eastwards over the Atlantic is lifted by low mountain ranges and produces orographic precipitation over and downstream of these coastal mountains. Suitable conditions for such events are often found within the warm sector of wintertime mid-latitude cyclones. These are

- prevailing fast low-level winds advecting a moist air mass (Browning et al., 1975), i.e. high values of integrated water vapour transport (IVT);
- Froude numbers larger than 1 that prevent blocking and divergence of the flow (Kunz and Kottmeier, 2006a);
- a roughly constant wind direction, such that the flow approaches the mountain range perpendicularly;
- a constant replenishment of moisture as a source of orographic clouds and precipitation (Browning et al., 1975);
- terrain sufficiently high to lift the boundary layer air mass above its lifting condensation level (Kunz and Kottmeier, 2006b).

If ocean temperature exceeds the atmospheric temperature above the sea surface, evaporation is favoured and

huge bands of moisture that transport water vapour from the Caribbean towards Europe can enhance the impact of the warm-sector precipitation. These so-called atmospheric rivers are the main precursors of extreme precipitation events in Europe and are expected to become more frequent and longer-lived, as well as more enriched with water vapour, in a warmer climate (Lavers and Villarini, 2015).

The Cumbria flood from 5 to 6 December 2015 caused severe flooding in the Lake District area in northern England (Marsh et al., 2016). This event is chosen as a case study due to its unprecedented intensity. The rainfall totals exceeded the previous 24 and 48 h UK records (Marsh et al., 2016). Surface temperatures exceeded 9 °C even at night, and strong winds with gust speeds of up to 40 ms<sup>-1</sup> were measured (Matthews et al., 2018; Marsh et al., 2016). Storm Desmond, which caused the Cumbria flood in 2015, was accompanied by an atmospheric river (Lavers et al., 2016) with peak 24 h mean IVT of more than 1100 kg m<sup>-1</sup> s<sup>-1</sup>, the highest observed for an atmospheric river impacting the British Isles since at least 1979 (Matthews et al., 2018). Figure 2a shows the mean wind direction during 6 h of the event. The moist flow approaches the Lake District mountains from the south-west with wind speeds of up to 40 ms<sup>-1</sup> in the lower troposphere (Fig. 2b). Orographically induced updrafts of more than 1 ms<sup>-1</sup> extend more than 4 km above sea level (a.s.l.). Correspondingly, downdrafts occur on the lee side of the hills.

The aims of this work are (1) to analyse the microphysical processes that enhance orographic rainfall in a mixed-phase cloud setting for the example of the Cumbria flood and (2) to analyse how these processes and their interaction change in a warming atmosphere and with changes in the concentration of CCN. The analysis is based on convection-permitting simulations with the Icosahedral Nonhydrostatic (ICON) model developed by the German Weather Service (Deutscher Wetterdienst, DWD) and the Max Planck Institute for Meteorology (Zängl et al., 2015) with an implementation of microphysical piggybacking (Grabowski, 2014). This method allows us to evaluate microphysical sensitivities without the potentially confusing impacts of changes in dynamics, radiation and other processes.

The article is structured as follows: Sect. 2 introduces the model setup, the piggybacking method as it is implemented in ICON and the budget equation that is used to analyse the results quantitatively. The results of the simulation are presented and analysed in Sects. 3 and 4. Section 5 provides a discussion of the results and compares them with other studies. The results are summarized in Sect. 6.

## 2 Methods

### 2.1 Model configuration

The simulations are performed with ICON version 2.5.0 (Zängl et al., 2015) with an implementation of the piggy-

backing approach, i.e. the ability to perform additional calls to the cloud microphysics scheme using perturbed input parameters. ICON is run in limited-area mode, with two domains (see Fig. 2b) nested into the standard ICON-EU grid (Reinert et al., 2022) based on DWD analysis data. The model works on an icosahedral grid to provide nearly homogeneous coverage of the globe. Boundary data are updated every 3 h for the simulations on the outer nest and every 15 min for the simulations on the inner nest. The outer nest has an average square-equivalent edge length of 1.6 km and covers most of the British Isles. The dynamical time step is 8 s. The simulation on the inner nest is initiated on 5 December 2015, 09:00 UTC (3 h after the start of the parent simulation), and is run for 27 h until 6 December 2015, 12:00 UTC. The inner nest extends from 4.2 to 1.8° W longitude ( $\approx$  155 km) and from 53.5 to 55.1° N latitude (180 km), covering the Lake District area in northern England, as shown in Fig. 2c. The triangular cells have an average square-equivalent edge length of 445 m, and the dynamical time step is 2 s. The inner nest has 125 vertical levels extending up to 23 km a.s.l. At this grid spacing, a 3D turbulence scheme (Dipankar et al., 2015; Heinze et al., 2017) is used. Shallow convection is parameterized (Bechtold et al., 2008), but no deep-convection scheme is used. The time step for the RRTM (Rapid Radiative Transfer Model) radiation scheme (Mlawer et al., 1997; Prill et al., 2022) is 720 s. The two-moment cloud scheme is used (Seifert and Beheng, 2006) with CCN activation parameterized as a function of vertical velocity (Hande et al., 2016).

### 2.2 Piggybacking method

Piggybacking is a simple and computationally efficient method to separate microphysical sensitivities from feedbacks to dynamics, radiation and other processes (Grabowski, 2014). It is motivated by a challenge that all sensitivity studies with fully interactive models encounter: perturbations of microphysical parameters cause feedbacks on the thermodynamic state of the atmosphere (e.g. on temperature and buoyancy by latent heating) and consequently on the dynamics of the system, i.e. wind, pressure and static stability, as well as radiative fluxes and turbulence. Here we use piggybacking (a) to quantify the immediate microphysical sensitivity of orographic rainfall to changes in thermodynamic conditions (here, changes in temperature) and (b) to investigate the response to changes in microphysical parameters, specifically the CCN number concentration.

The implementation of piggybacking applied in this study adds four sets of all microphysical prognostic variables to the model. Each set represents an individual simulation of cloud microphysics, driven by the same dynamic fields as the reference simulation. The cloud microphysics scheme is called five times per time step, once for the reference simulation and once for each of the four piggybacking sets. Thus, at each time step, all of the five microphysical-variable sets are

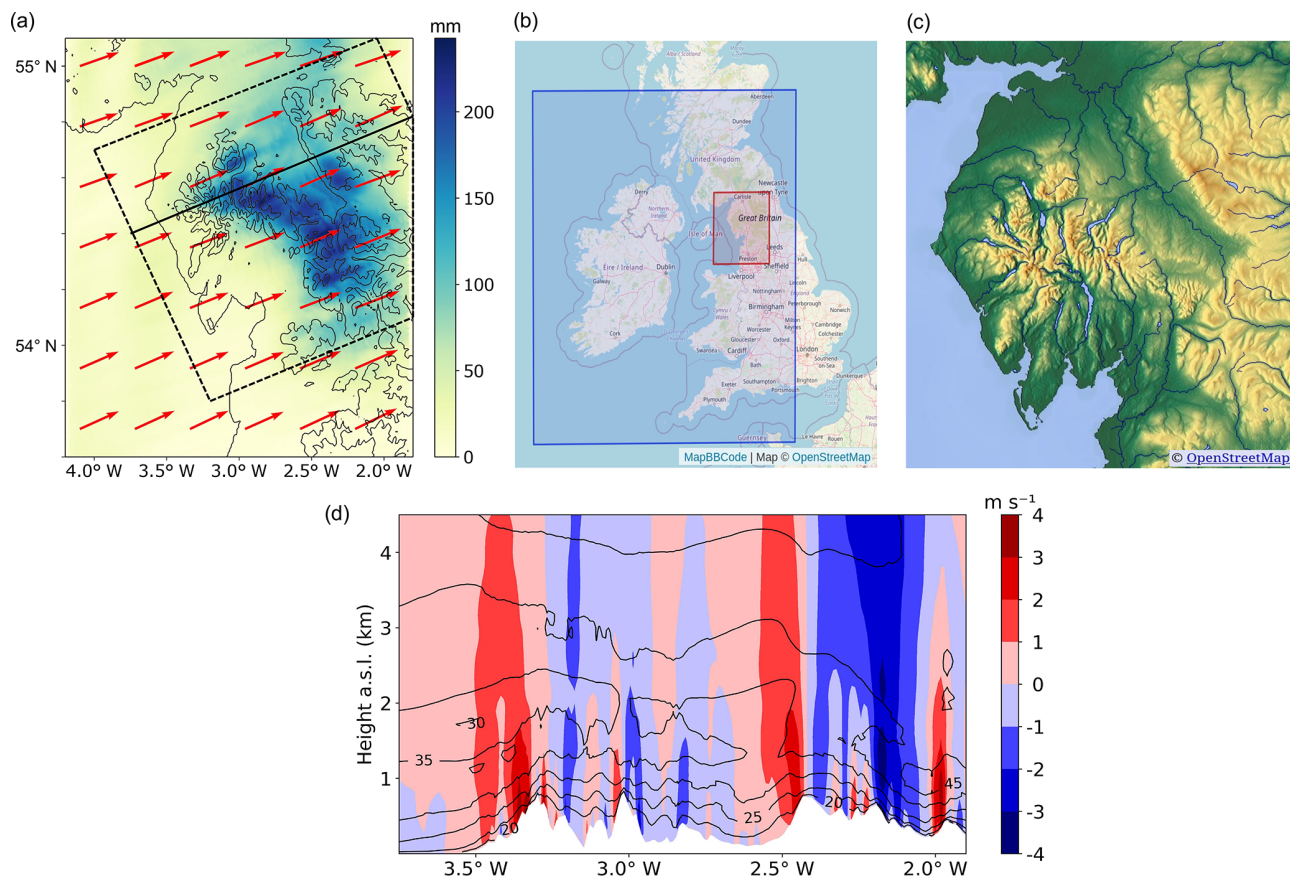


**Figure 2.** (a) The 24 h accumulated surface rainfall (5 December 2015, 10:00 UTC, to 6 December 2015, 10:00 UTC) on the inner nest. Dashed black polygon: evaluation domain (LAKEDISTR); solid black line: cross section used in panel (d) and in Sect. 3.2; red arrows: 6 h (period indicated in Fig. 3) average wind direction at 1.5 km a.s.l. (b) Map of outer and inner nest. (c) Topography of the inner nest. The highest peaks are approximately 1 km high. (d) Up- and downdraft (red and blue shading) and horizontal wind speed (black contours) at 18:00 UTC interpolated to 200 evenly spaced points along the cross section in panel (a). © OpenStreetMap contributors. Distributed under the Open Data Commons Open Database License (ODbL) v1.0.

updated. Therefore, each simulation results in five complete output variable sets with different microphysics but identical wind (see Fig. 2a and d) and pressure fields. In this work, the perturbed parameters are virtual potential temperature  $\Theta_v$  and the surface CCN concentration  $n_{CCN}$ .  $\Theta_v$  instead of absolute temperature is used to preserve static stability.  $n_{CCN}$  determines the vertical CCN profile (Hande et al., 2016). Except for  $\Theta_v$  and specific humidity  $q_v$  (in the temperature sensitivity experiments), the microphysical-variable sets are initialized identically. The  $\Theta_v$  and  $q_v$  fields slowly diverge due to differences in calculated microphysical process rates resulting from the different (prognostic) temperature or (diagnostic) CCN concentration. Initially,  $q_v$  is adjusted to the perturbed value of  $\Theta_v$  such that relative humidity (RH) is identical to the reference simulation when the piggybacked simulation is initialized. This adjustment is motivated by the assumption that an increase in global temperature is accompanied by an increase in sea surface evaporation, such that RH will not change significantly in the future climate (Pört-

ner et al., 2022). For simplicity, perturbations of  $\Theta_v$  are referred to as *temperature perturbations* throughout the paper.

Perturbations are chosen such that they resemble extreme but realistic deviations from the reference state. Warming and cooling scenarios are simulated by adding a constant offset of  $\Delta\Theta_v = \pm 1$  K and  $\Delta\Theta_v = \pm 3$  K to the virtual potential temperature field in the microphysics scheme (and only there). To account for different degrees of atmospheric pollution, the initial value  $n_{CCN} = 500$  cm<sup>-3</sup> has been rescaled by a factor of 0.1 and 0.4 to represent clean, maritime conditions and by a factor of 1.6 and 3 to represent polluted conditions. The resulting range of surface CCN concentration is thus  $n_{CCN} = 50, 200, 500, 800$  and  $1500$  cm<sup>-3</sup>. In total, 25 simulations have been run, 1 for each combination of temperature and CCN perturbations. The simulations are denoted as PB- $T$ -CCN, where  $T$  is the value of  $\Delta\Theta_v$  in kelvin (K) and CCN is the value of  $n_{CCN}$  in inverse cubic centimetres (cm<sup>-3</sup>). Thus, PB-0-500 denotes the reference simulation that provides the dynamics for all other simulations. An

additional set of four simulations with temperature perturbations  $\Delta\Theta_v = \pm 2\text{ K}$  and  $\Delta\Theta_v = \pm 4$  and  $n_{\text{CCN}} = 500\text{ cm}^{-3}$  together with the five PB-T-500 simulations is referred to as PB-T ( $-4\text{ K} \leq \Theta_v \leq +4\text{ K}$ ).

## 2.3 Analysis methods

### 2.3.1 Sensitivity decomposition

The function  $\alpha_X(\Theta_v)$  with units  $\% \text{ K}^{-1}$  defined as

$$\alpha_X(\Theta_v) = \frac{1}{X} \frac{\partial X}{\partial \Theta_v} \cdot 100\% \quad (1)$$

is called the temperature sensitivity of quantity  $X$ . If there is no significant feedback, the dynamical, thermodynamic and microphysical contributions to the total sensitivity can be linearly decomposed. For the sensitivity to total surface rainfall,  $P$ , this decomposition reads

$$\alpha_P(\Theta_v) = \frac{1}{P} \frac{\partial P}{\partial \Theta_v} \Big|_{\text{dyn}} + \frac{1}{P} \frac{\partial P}{\partial \Theta_v} \Big|_{\text{thermodyn}} + \frac{1}{P} \frac{\partial P}{\partial \Theta_v} \Big|_{\text{mphys}} \quad (2)$$

Using the piggybacking method, the first term on the right-hand side of Eq. (2), the dynamical contribution, vanishes, since the dynamical fields are identical in each simulation. The term with index *thermodyn* corresponds to changes in rainfall caused by the increase in water vapour inflow,  $I$ , and its condensation onto cloud droplets and deposition onto ice or snow ( $C$ ), referred to as thermodynamic contribution. The index *mphys* refers to changes in the processing of cloud condensate,  $C$ , and precipitation formation (microphysical contribution). Since this work focuses on rain formation, the important microphysical processes are those related to rain generation (autoconversion; accretion, i.e. collision–coalescence between cloud droplets and raindrops; and melting) and rain removal (riming of raindrops onto snow or graupel, evaporation of raindrops).

### 2.3.2 Evaluation domain and time averaging

The dashed black contours in Fig. 2a outline the evaluation domain, which is aligned with the mean wind speed and is referred to as LAKEDISTR. Figure 3 shows the simulated hourly rates of surface rainfall, averaged over LAKEDISTR. The solid blue line marks the 16 h period used to calculate all totals defined in the following section. Starting on 5 December 2015, 10:00 UTC, and ending on 6 December 2015, 02:00 UTC, it is chosen such that it includes the highest rainfall rates and ends before a rapid decrease in rainfall is observed. The 24 h period (dashed) is used to calculate the accumulated surface rainfall in Sect. 3.1. For computational efficiency, cloud content and process rates in Sect. 3.2 to 3.4 are averaged over a shorter time period (13:00 to 19:00 UTC)

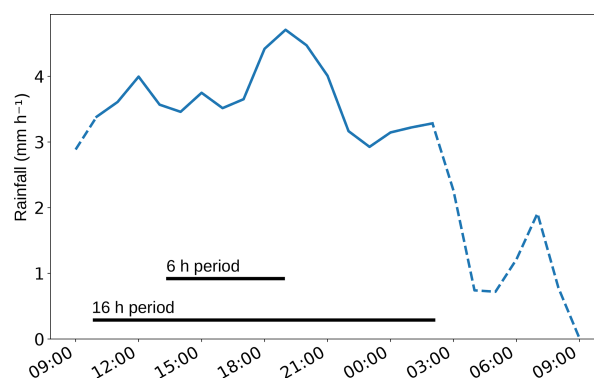


**Figure 3.** Hourly rainfall integrated over LAKEDISTR, starting on 5 December 2015, 10:00 UTC. The solid blue line indicates the 16 h period used to calculate the totals in Sect. 4. Solid black lines: time periods used to average data.

from 5 min data output. The results are qualitatively the same as for the 24 h period (not shown).

### 2.3.3 Budget equation for total surface rainfall

The production of orographic rainfall can be decomposed into several phases: (1) the water vapour inflow, (2) the formation of an orographic cloud, and (3) the microphysical processing inside the cloud that eventually leads to formation and sedimentation of orographic rainfall. The amount of surface rainfall  $P$  is related to the total water vapour inflow  $I$  by the dimensionless drying ratio:

$$\text{DR} = \frac{P}{I} \quad (3)$$

$I$  is the integrated water vapour flux through the southwestern boundary of LAKEDISTR, averaged over the 16 h period shown in Fig. 3. All totals introduced in this section are given in kilograms, such that the respective efficiencies are dimensionless. The following considerations are adapted from Kirshbaum and Smith (2008).

After the moist air enters LAKEDISTR (phase 1), it is forced to ascend over the mountain barrier. After saturation is reached, a part of it forms liquid (or ice) condensate (phase 2). The total amount of cloud condensate  $C$  created this way is related to  $I$  by the condensation ratio:

$$\text{CR} = \frac{C}{I} \quad (4)$$

The fraction of cloud condensate that is converted into rain and reaches the surface (phase 3) is called precipitation efficiency:

$$\text{PE} = \frac{P}{C} \quad (5)$$

With the three efficiencies DR, CR and PE defined,  $P$  can be expressed as

$$P = I \cdot \text{DR} = I \cdot \text{CR} \cdot \text{PE} \quad (6)$$

The temperature sensitivity of total surface rainfall (see Eq. 2) can now be written as follows:

$$\begin{aligned}\alpha_P &= \frac{1}{P} \frac{\partial P}{\partial \Theta_v} \Big|_{\text{dyn}} + \frac{1}{I} \frac{\partial I}{\partial \Theta_v} + \frac{1}{\text{CR}} \frac{\partial \text{CR}}{\partial \Theta_v} + \frac{1}{\text{PE}} \frac{\partial \text{PE}}{\partial \Theta_v} \\ &= \alpha_{P,\text{dyn}} + \alpha_I + \alpha_{\text{CR}} + \alpha_{\text{PE}} \\ &= \alpha_I + \alpha_{\text{CR}} + \alpha_{\text{PE}} \quad (\text{with piggybacking}).\end{aligned}\quad (7)$$

Here, all dynamical feedbacks are summarized in  $\alpha_{P,\text{dyn}}$ , while  $\alpha_I$ ,  $\alpha_{\text{CR}}$  and  $\alpha_{\text{PE}}$  contain the microphysical and thermodynamic contributions. If CR and PE were unchanged in the different temperature and CCN scenarios, the amount of surface rainfall would increase proportionally to the amount of atmospheric water vapour in the inflow ( $\alpha_I$ ). The leading question of this work is to what extent the temperature sensitivity of  $P$  deviates from the Clausius–Clapeyron scaling, i.e. how CR and PE change with temperature and which processes are responsible for their change. Furthermore, the effect of changing the CCN concentration at different temperature scenarios shall be investigated.

The microphysical processing within the cloud can further be decomposed by defining a rain generation total,

$$G = \text{autoconversion} + \text{accretion} + \text{melting}, \quad (8)$$

and a rain loss total,

$$L = \text{rain riming} + \text{rain evaporation}. \quad (9)$$

If lateral in- and outflow and initial condensate are negligible,  $P$  equals the difference  $G - L$ .

### 3 Results

#### 3.1 Spatial distribution of surface rainfall

Figure 4 shows the 24 h accumulated rainfall on the inner nest for the reference and the  $\pm 3$  K cooling and warming scenarios. The area that experiences extreme rainfall ( $> 200$  mm) increases as the atmosphere warms, while the distribution of light rainfall ( $< 100$  mm) appears mainly unchanged. Notably, the area around the mountain ridge experiences the strongest increase in rainfall. To quantify the observed changes, Fig. 5a shows the hourly rainfall rate  $p$  inside LAKEDISTR as well as the rate above 600 m ( $p_{\text{ridge}}$ ) and below 150 m ( $p_{\text{low}}$ ) for temperature deviations of  $-4$  to up to  $+4$  K from the reference state.  $p$  increases gradually at a rate of  $1.6\% \text{ K}^{-1}$ . In contrast,  $p_{\text{ridge}}$  increases at  $6.0\% \text{ K}^{-1}$  (close to CC scaling), whereas  $p_{\text{low}}$  decreases at  $-1.1\% \text{ K}^{-1}$ . Figure 5b shows that the values of  $p_{\text{ridge}}$  are within the 90th and 95th percentile of total rainfall at all grid cells inside LAKEDISTR and that  $p_{\text{low}}$  changes with temperature similarly to the 60th percentile. Both panel (a) and panel (b) in Fig. 5 reveal that regions with already high rainfall rates experience the strongest increase in rainfall with

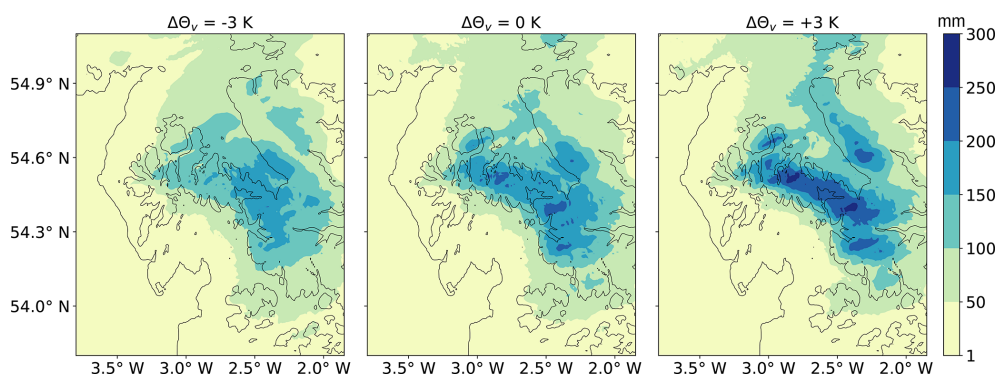
warming, whereas regions with low rainfall rates in the PB-0-500 simulation experience a gradual change with temperature or even decreasing rainfall rates. It is noteworthy that the numbers shown in Fig. 5 depend on the choice of the integration domain and time period (not shown), but the qualitative results do not. The processes causing the orographic rain enhancement are disentangled in the next sections.

#### 3.2 Cloud hydrometeor distribution along a vertical cross section

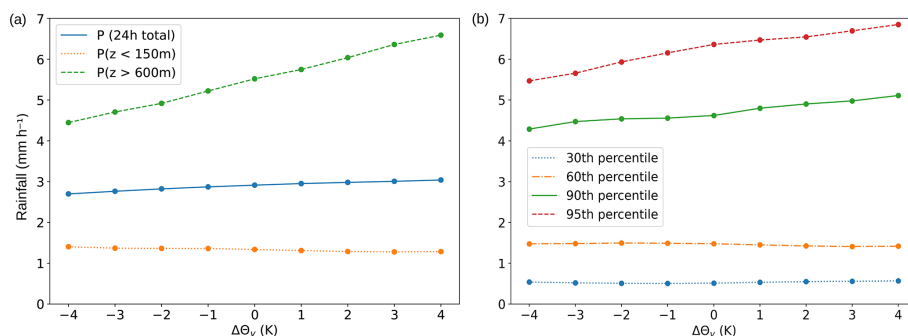
A comprehensive picture of the cloud distribution and the rain-generating processes involved is given in Fig. 6 for three different temperature scenarios. Shown are filled contours of frozen (a) and liquid (c) cloud water content together with contours of melting and accretion rates (e). Below each contour plot, column-integrated values of water content (b, d) or microphysical process rates (f) are displayed. Panel (g) shows vertical profiles of rain generation and removal processes for each scenario. As in Fig. 4, results of the  $\pm 3$  K cooling and warming scenarios are compared with the reference simulation. All values in Fig. 6 are averaged over the 6 h period starting at 13:00 UTC and evaluated along the vertical cross section indicated in Fig. 2, aligned with the mean wind. The cross section cuts through the Lake District as well as the subsequent mountain range (the Pennines).

Figure 6a shows the distribution of ice, snow and graupel. Although the cold cloud extends up to 9 km a.s.l., it is initiated orographically by the first steep slope of the Lake District mountains at 30 km distance from the coast. The cloud ice located between 6 km and 8 km a.s.l. is mostly unaffected by the temperature change, indicated in the comparison of the column-integrated values in row (b). The amount of snow and graupel decreases as the temperature is increased from  $-3$  to  $+3$  K with respect to the reference simulation, mostly due to the rise of the melting level from just below 1.5 km in the cooling case to 3 km in the warming case. The additional liquid condensate in the warming scenario then contributes to the liquid cloud content, as can be deduced from Fig. 6d. The replacement of frozen water content by liquid has two opposite effects on rain production: enhancement of warm-rain production via collision–coalescence and reduction in cold-rain formation via the Wegener–Bergeron–Findeisen process and riming.

The liquid water path (LWP) has maxima above each ridge (Fig. 6d). In the cooling scenario, the liquid cloud water shown in Fig. 6c extends far downstream into the valley, while it is partially evaporated and partially converted into rainwater above the valley in the warming scenario. The LWP at the eastward ridge is largely unchanged in the three temperature scenarios. This suggests that the additional moisture contained in a warmer atmosphere is washed out before it is able to be advected downstream. A comparison of the competing effects – washout of cloud water and evaporation of rain – is made in Sect. 4.



**Figure 4.** The 24 h (5 December 2015, 10:00 UTC, to 6 December 2015, 10:00 UTC) accumulated rainfall for three PB-*T*-500 simulations. Black contours indicate the orography at 1 m, 250 m and 500 m a.s.l.



**Figure 5.** (a) Average 24 h rainfall rate evaluated inside LAKEDISTR ( $p$  in solid blue,  $p_{\text{ridge}}$  in dashed green,  $p_{\text{low}}$  in dotted orange) for the PB-*T* simulations with  $-4\text{ K} \leq \Delta\Theta_v \leq +4\text{ K}$ . (b) The 30th, 60th, 90th and 95th percentile for the PB-*T* simulations.

### 3.3 Distribution of rain production processes

To determine which rain generation effect dominates and how atmospheric warming affects the interplay of cold- and warm-rain production, a detailed look at the associated microphysical processes is necessary. Figure 6e and f display average rates of melting and accretion. These two processes quantify the main contributions to cold- and warm-rain production, respectively. Condensational growth of droplets and cloud droplet–cloud droplet collection (autoconversion) are negligible warm-rain processes compared to the accretion of cloud droplets by raindrops. In the warming and cooling scenarios, the melting region is lifted or lowered according to the melting level. The two maxima of vertically integrated melting rates (Fig. 6f) decrease with temperature and are additionally shifted upwind in the warming case. In contrast, the amount of accretion increases significantly with temperature, with two distinct accretion maxima over each first peak of the mountain range. As the liquid cloud top extends further upwards in the warmer scenarios, the accretion region does too, thereby increasing the value of the accretion maxima, without changing their location. In line with the liquid cloud water distribution, there is almost no accretion occurring over the valley.

The observed occurrence of melting and accretion can be explained considering typical timescales of cold- and warm-rain processes. Melting of graupel, which is the dominating cold-rain contribution, requires riming of liquid water droplets onto graupel or freezing of rain. The relatively long chain of processes, leaving time for horizontal advection caused by wind speeds of  $30\text{--}40\text{ m s}^{-1}$  (Fig. 2b), leads to the observed distribution of melting with a maximum located far downwind of the mountain peaks. Accretion, on the other hand, is most effective in the region of maximum LWC. The altitude of maximum LWC is close to the mountain top (between 1 km and 2 km a.s.l. in the reference and warming scenario), such that most of the rain produced in that region is deposited around the peaks. The plateau-like pattern downstream of the first accretion maximum is caused by the accretion of cloud droplets by melted graupel particles from the mixed-phase cloud.

The vertical profiles in Fig. 6g show that melting of graupel contributes most to the rain generation budget. Autoconversion is the least important process and is highest in the warming scenario, where more cloud water is available. Both riming and melting decrease with warming, and their maximum is lifted according to the melting level. Rain evaporation increases as the total rain generation, i.e. the sum of

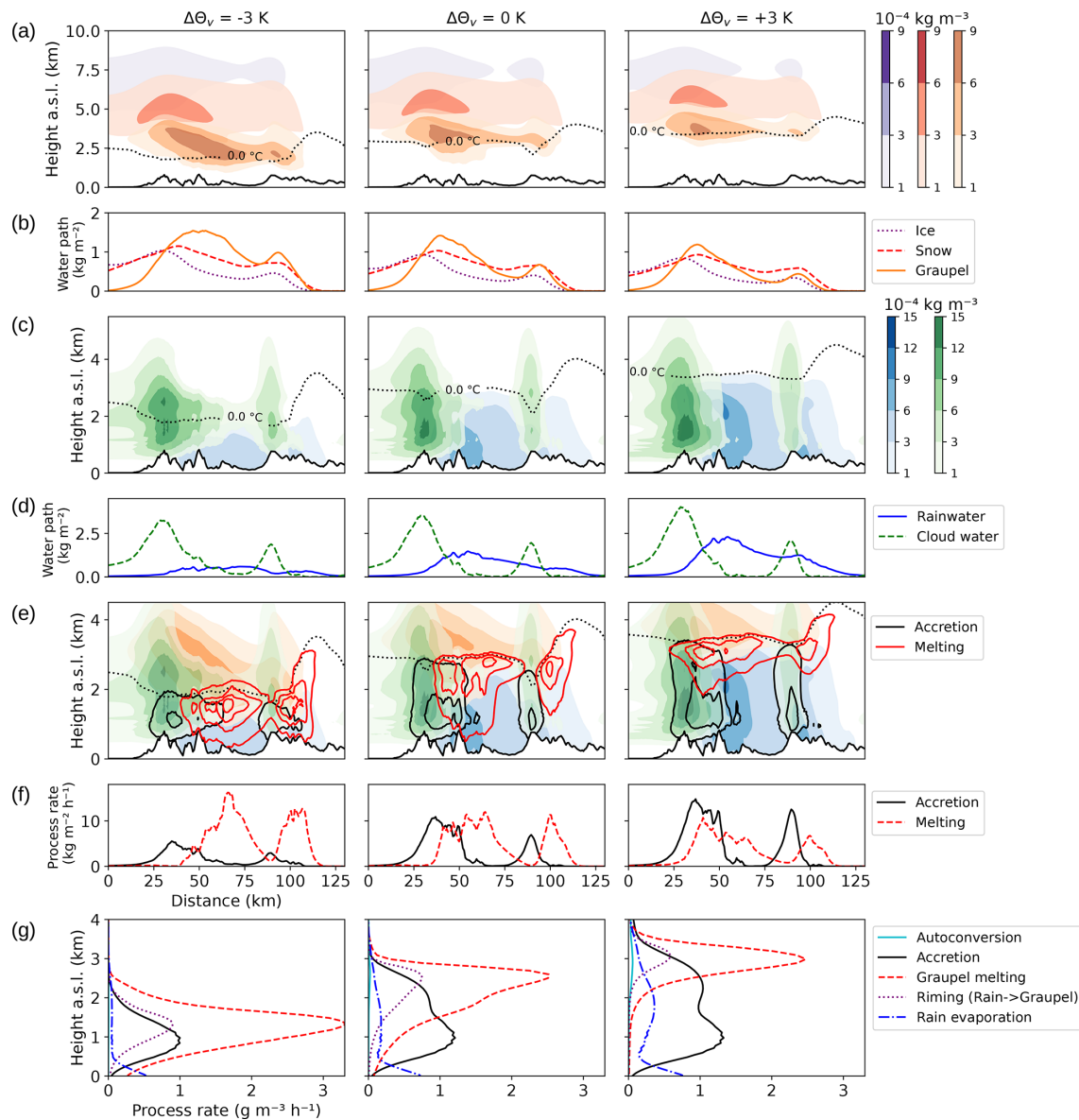


**Figure 6.** (a) Filled contours of ice (purple), snow (red) and graupel (orange) content along the cross section shown in Fig. 2a. (b) Column-integrated values of the data presented in row (a). (c) Filled contours of cloud water (green) and rainwater (blue) along the same cross section. (d) Column-integrated values of the data presented in row (c). (e) Filled contours of graupel (orange), cloud (green) and rainwater (blue) as in rows (a) and (c) together with contours of the melting rate (red lines) and accretion rate (blue lines) at  $\{1, 5, 10, 15\} \text{ g m}^{-3} \text{ h}^{-1}$ . (f) Column-integrated values of melting and accretion data presented in row (e). (g) Vertical profiles of processes contributing to rain generation or rain removal. Values are evaluated inside LAKEDISTR. Columns correspond to the  $\Delta\Theta_v = -3 \text{ K}$  (left),  $\Delta\Theta_v = 0 \text{ K}$  (middle) and  $\Delta\Theta_v = +3 \text{ K}$  (right) simulations. All values are 6 h averages (from 5 December 2015, 13:00 UTC). Orography is outlined at the bottom of row (a), (c) and (e).

autoconversion, accretion and melting, increases. Accretion increases strongly in a warming atmosphere, as the melting level rises and the liquid cloud layer extends vertically. A second maximum in the vertical profile of the accretion rate forms slightly below the melting level, visible in the reference and warming scenarios. The maxima correspond to levels of high LWC (horizontally averaged).

### 3.4 Raindrop trajectories

Figure 7 shows estimated raindrop trajectories starting at the melting level together with the mean rainwater flux between 13:00 and 19:00 UTC. The trajectory endpoints are chosen every 10 km starting at 50 km distance from the coast. The rainwater flux is calculated from the rainwater mixing ratio  $qr$  weighted with mass mean fall velocity in each grid cell,



which is calculated as the sum of the updraft  $w$  and the terminal velocity used in the microphysics scheme of the model (Seifert and Beheng, 2006). The terminal velocity is parameterized as a power law for the mean raindrop mass ( $qr/qnr$ ). The fall velocity then reads

$$v_{\text{fall}} = w + 159.0 \cdot \left( \frac{qr}{qnr} \right)^{0.266} \cdot \left( \frac{\rho}{\rho_0} \right)^{0.5} \text{ ms}^{-1}, \quad (10)$$

with  $\rho_0 = 1.255 \text{ kg m}^{-3}$  and air density  $\rho$ . Maxima of rainwater flux are located above the highest peaks. The trajectories associated with these high rainwater fluxes pass through regions where melting and accretion coincide or where accretion occurs below the melting layer. Such cases, where melting and accretion are spatially separated but occur along the trajectory of falling hydrometeors yield the most efficient rain enhancement, e.g. for the 50 km trajectory in Fig. 7g.

#### 4 Budget analysis

The first part of this section quantifies the relative importance of rain generation and removal processes. In the second part, the total rainfall is decomposed using the efficiencies introduced in Sect. 2.3. This allows us to determine how efficiently water vapour is converted into surface rainfall and how the three phases of rain production – water vapour inflow, hydrometeor formation and microphysical processing – change individually when the atmosphere warms. All totals are evaluated inside LAKEDISTR. Temperature sensitivities are given for the relative change between the +3 K warming scenario with intermediate CCN concentration (PB-plus3-500) and the reference simulation (PB-0-500), i.e.  $\alpha_X = \alpha_X(3 \text{ K})$ . The temperature sensitivities obtained from all other PB- $T$ -CCN simulations are listed in Appendix A in Tables A1–A8.

##### 4.1 Microphysical processes and surface rainfall budget

Figure 8 shows integrated values of all rain generation and loss processes as well as their sum together with total rainfall  $P$  and total water vapour inflow  $I$  obtained from the PB- $T$ -CCN simulations.  $I$  is 1 order of magnitude larger than  $P$  and increases by  $\alpha_I = 5.88 \text{ \% K}^{-1}$  in the +3 K warming scenario (independent of CCN concentration).  $P$  (16 h total) increases by only  $\alpha_P = 0.03 \text{ \% K}^{-1}$ . The reason for this difference between  $\alpha_I$  and  $\alpha_P$  is examined in Sect. 4.2. The rain budget  $G - L$  overestimates  $P$  in the warming cases and slightly underestimates it in the cooling cases, with relative deviations of less than  $\pm 5 \text{ \%}$ . This might be due to the exclusion of in- and outflow of rainwater through the boundaries of LAKEDISTR.

Consistent with the vertical profiles shown in Fig. 6g, autoconversion increases with temperature ( $\alpha_{\text{auto}} = 87.29 \text{ \% K}^{-1}$ ) but is only a minor contribution to rain generation. It is more efficient when fewer CCN

particles are available. Rain evaporation increases by  $\alpha_{\text{evap}} = 25.88 \text{ \% K}^{-1}$ , due to more rainwater being available, while riming of raindrops in the mixed-phase cloud region decreases, due to the lifted melting level and reduced graupel content. Melting and accretion dominate the rain generation budget. While accretion is significantly enhanced as the air gets warmer, increasing by  $\alpha_{\text{acrr}} = 14.96 \text{ \% K}^{-1}$ , melting is reduced by  $\alpha_{\text{melt}} = -7.22 \text{ \% K}^{-1}$  but remains almost as important as accretion even in the +3 K scenario. Reducing the CCN concentration from  $500$  to  $200 \text{ cm}^{-3}$  (without perturbing  $\Theta_v$ ) yields only a  $0.93 \text{ \%}$  increase in total rainfall, although accretion is enhanced by  $8.64 \text{ \%}$  (not shown).

Altogether, the accretion enhancement (warm-rain formation) cannot counteract the decrease in melting (a proxy for mixed-phase precipitation formation) and the increased rain removal by evaporation ( $25.88 \text{ \% K}^{-1}$ ) in a warmer atmosphere. Therefore, the surface rainfall increases much less than the total water vapour inflow. In each temperature scenario, a cleaner atmosphere enhances all microphysical processes shown.

##### 4.2 Precipitation efficiency, condensation and drying ratio

Following the definitions given in Sect. 2.3, the total rainfall integrated over LAKEDISTR can be written as the water vapour inflow  $I$  multiplied by the drying ratio DR, which is the product of the condensation ratio CR and precipitation efficiency PE. This decomposition helps to separate cloud microphysical processes (determining PE) from atmospheric thermodynamics (the main driver of CR) and to analyse their sensitivities individually. Figure 9 shows the efficiencies DR, CR and PE as functions of  $\Delta\Theta_v$  for three values of  $n_{\text{CCN}}$ . In the PB-0-500 case, CR = 30 % of the inflowing water vapour is converted into cloud condensate. From the total condensate, PE = 34 % reaches the ground as surface rainfall. The product DR = CR · PE shows that 10 % of the inflowing moisture sediments as rain to the surface (see also Fig. 8). The temperature sensitivities of these ratios are discussed in the following.

$I$  increases at a lower rate ( $\alpha_I = 5.88 \text{ \% K}^{-1}$ ) than the CC scaling in the temperature range of the Cumbria case ( $6.5 \text{ \% K}^{-1}$  to  $7.5 \text{ \% K}^{-1}$ , Fig. 1) because the increase in absolute temperature is lower than the prescribed 3 K increase in  $\Theta_v$ . The partial derivative  $\partial T / \partial \Theta_v$  ranges between 1 (at the ground) and 0.75 (at 8 km a.s.l.). Therefore, the actual temperature sensitivity of  $I$  is between  $5.88 \text{ \% K}^{-1}$  and  $7.84 \text{ \% K}^{-1}$  but is not calculated here explicitly.

The condensation ratio CR =  $C/I$  decreases with increasing temperature ( $\alpha_{\text{CR}} = -3.39 \text{ \% K}^{-1}$ ). This is because the condensation total  $C$ , including condensation and deposition, increases with warming by only  $1.89 \text{ \% K}^{-1}$  (not shown). As mixed-phase processes play an important role in the Cumbria case, this value is the result of two counteracting effects with the same order of magnitude. The condensation rate ob-

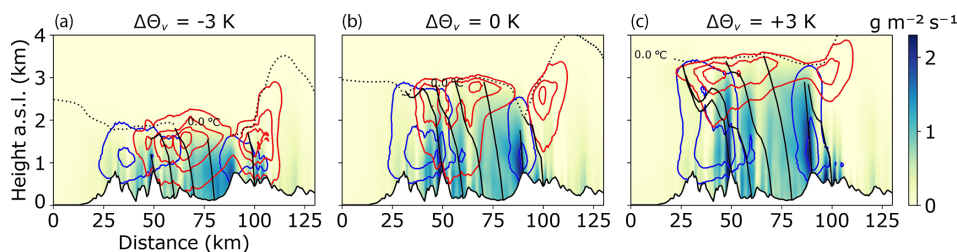


**Figure 7.** Rainwater flux (shading) and raindrop trajectories (black) at 18:30 UTC (shading) together with contours of 6 h averaged melting (red) and accretion (blue) rates at  $\{1, 5, 10, 15\} \text{ g m}^{-3} \text{ h}^{-1}$ . The panels show the  $\Delta\Theta_v = -3 \text{ K}$  (a),  $\Delta\Theta_v = 0 \text{ K}$  (b) and  $\Delta\Theta_v = +3 \text{ K}$  (c) simulations. Orography is displayed at the bottom.

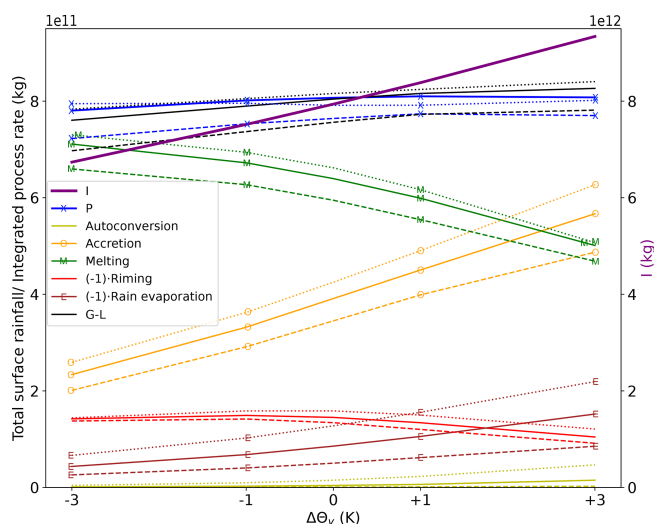


**Figure 8.** Processes contributing to rain generation (autoconversion, accretion and melting) and removal of rain (rain evaporation, riming onto graupel) for four temperature perturbations at three different CCN concentrations,  $n_{\text{CCN}} = 200 \text{ cm}^{-3}$  (dotted),  $500 \text{ cm}^{-3}$  (solid) and  $1500 \text{ cm}^{-3}$  (dashed). The values are averaged over 16 h and integrated inside LAKEDISTR, as defined in Sect. 2.3. Black lines show the sum of the rain generation processes minus the sum of the removal processes ( $G - L$ ). Blue lines show the 16 h rainfall total  $P$ . The purple line shows the integrated water vapour inflow  $I$  for all CCN concentrations. Values of  $I$  are shown on the right axis.

tained from saturation adjustment only, i.e. the total increase in LWC from condensational growth, yields a sensitivity of  $5.44 \% \text{ K}^{-1}$ , similar to the change in  $I$ . In contrast, the total water vapour deposition to ice particles inside LAKEDISTR decreases by  $-4.50 \% \text{ K}^{-1}$ . The negative sensitivity of depositional growth leads to the low value of the sensitivity of  $C$  and explains the negative sensitivity of CR.

While rain generation is most efficient at high temperature perturbations, the precipitation efficiency PE decreases by  $\alpha_{\text{PE}} = -1.76 \% \text{ K}^{-1}$ , which is explained by the strong increase in rain loss ( $3.74 \% \text{ K}^{-1}$ ), driven mainly by enhanced evaporation. That means, the total amount of condensate (with an increased liquid fraction) is converted to surface

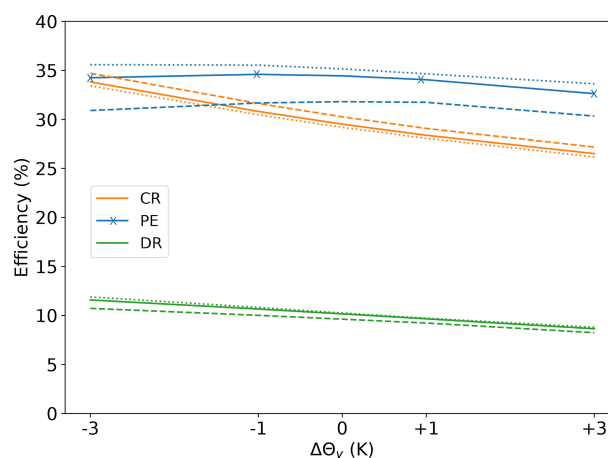


**Figure 9.** Efficiencies in percent (%) as defined in Sect. 2.3 for the PB-T-CCN simulations. Values at three different CCN concentrations  $n_{\text{CCN}} = 200 \text{ cm}^{-3}$  (dotted),  $500 \text{ cm}^{-3}$  (solid) and  $1500 \text{ cm}^{-3}$  (dashed) are plotted over  $\Delta\Theta_v$ . Colours indicate the condensation ratio (orange), precipitation efficiency (blue), and drying ratio (green).

rainfall less efficiently in a warmer atmosphere. As a result, the drying ratio decreases by  $\alpha_{\text{DR}} = -4.97 \% \text{ K}^{-1}$ .

The condensation ratio CR is larger for high CCN concentration but has the same temperature sensitivity (see Table A6). This is due to enhanced condensation for high CCN concentration over the second mountain range. Since less water is washed out of the cloud in the polluted scenario, more moisture is advected downstream and can be condensed again, increasing  $C$ . The precipitation efficiency PE on the other hand is lower in the polluted scenario (Table A7), due to smaller droplets and reduction in the accretion efficiency. Furthermore, smaller droplets are more easily evaporated once they are advected to the lee of the mountain. The two (CR and PE) effects counteract each other, such that the CCN sensitivity of the drying ratio DR is lower than the individual sensitivities of CR and PE. However, the PE sensitivity dominates, such that DR decreases with increasing CCN concentration consistently in all temperature perturbation scenarios (Table A8).

### 4.3 Separating sensitivities in simulations with combined temperature and CCN perturbations

The total rainfall produced in the simulations with combined CCN and temperature piggybacking (PB-*T*-CCN) is analysed in this section. The 25 simulations are all driven by the dynamic fields of the reference simulation PB-0-500, with which the PB-*T*-CCN simulations are compared. The aim of this analysis is to (a) estimate the relative importance of changing CCN concentration compared to an increase in temperature and (b) identify whether the changes in  $P$  in the PB-*T*-500 and PB-0-CCN simulations are linearly independent.

Let  $P_{X,Y}$  be the 24 h rainfall total in any PB- $X$ - $Y$  simulation, where  $X$  denotes the temperature perturbation  $\Delta\Theta_v$  in kelvin (K) and  $Y$  the CCN concentration  $n_{\text{CCN}}$  in inverse cubic centimetres ( $\text{cm}^{-3}$ ) and  $P_{0,500}$  is the 24 h rainfall total in the reference simulation (PB-0-500). Then

$$\Delta P_{X,Y} = P_{X,Y} - P_{0,500} \quad (11)$$

is the absolute difference in rainfall in any PB- $X$ - $Y$  simulation from the reference simulation. The individual contributions from the PB-*T* and PB-CCN simulations are then

$$\Delta P_X^{\Delta T} = P_{X,500} - P_{0,500}, \quad (12)$$

$$\Delta P_Y^{\text{CCN}} = P_{0,Y} - P_{0,500}. \quad (13)$$

Values for  $\Delta P_{X,Y}$  (normalized by  $P_{0,500}$ ) are shown in Fig. 10a. The relative deviations vary from  $-13\%$  for the coolest and most polluted scenario to  $+7\%$  in the warmest and cleanest scenario. Consistently, at all temperature perturbations, an increase in CCN concentration yields a decrease in  $P$ , and at all CCN perturbations, an increase in temperature results in an increase in  $P$ . Table 1 shows the temperature sensitivities  $\alpha_P$  calculated for the four perturbations of  $\Theta_v$  with respect to the reference simulation at fixed CCN concentration. Simulations run in more polluted scenarios ( $n_{\text{CCN}} = 800$  and  $1500 \text{ cm}^{-3}$ ) have systematically higher sensitivities than the simulations under cleaner conditions ( $n_{\text{CCN}} = 50$  and  $200 \text{ cm}^{-3}$ ), due to smaller drop sizes as well as a different partitioning of warm- and cold-phase processes and a resulting less negative sensitivity of PE (see Fig. 9 and Table A7). The sensitivities vary between  $0.5\% \text{ K}^{-1}$  and  $2.4\% \text{ K}^{-1}$  but are still much smaller than the CC scaling.

If feedback of temperature change on CCN concentration and vice versa are negligible, the PB-*T* and PB-CCN contributions can be used to calculate the rainfall totals as a linear combination:

$$P_{X,Y}^{\text{lin}} = \Delta P_X^{\Delta T} + \Delta P_Y^{\text{CCN}} + P_{0,500}. \quad (14)$$

To analyse to what extent this sum deviates from the combined effect  $P_{X,Y}$ , the relative error

$$\delta P_{X,Y}^{\text{lin}} = \frac{P_{X,Y}^{\text{lin}} - P_{X,Y}}{P_{X,Y}} \quad (15)$$

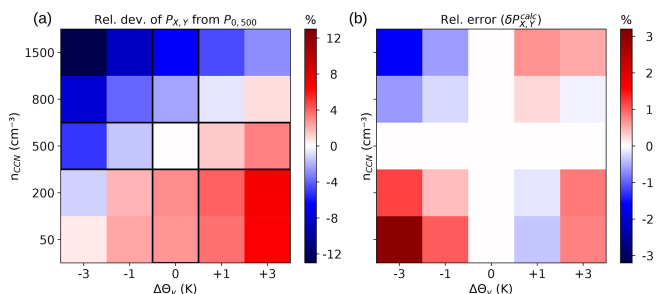


**Figure 10.** (a) Relative change in average 24 h rainfall in the PB-*T*-CCN simulation w.r.t. the reference simulation (PB-0-500). (b) Relative error of (by linear combination) calculated rainfall totals for the PB-*T*-CCN simulations.

is shown in Fig. 10b. The calculated rainfall deviates from the simulated rainfall by less than 3%. In the warming scenarios, deviations are smaller and there is no systematic over- or underestimation. In the cooling scenarios, adding the individual contribution at reduced CCN concentration causes an underestimation of the produced rainfall, and doing so at increased CCN concentration yields an overestimation. However, the individual CCN and temperature contributions can be used to estimate the total rainfall for an arbitrary combined scenario at  $\pm 3\%$  accuracy. This finding supports piggybacking as a powerful method to separate thermodynamic and microphysical sensitivities.

## 5 Discussion

In this section the results shown in Sects. 3 and 4 are discussed and compared with the literature. In addition, limitations and possible extensions are discussed.

### 5.1 Interpretation and comparison

The interplay of cold- and warm-rain processes in the Cumbria flood case can be characterized as a *mixed-phase* seeder–feeder mechanism. The rain enhancement is strongest when melted hydrometeors from the mixed-phase region serve as seeder particles that collect cloud droplets from the liquid (feeder) cloud region below. Cases in which the melting and accretion regions are vertically separated yield the most efficient rain enhancement because accretion can efficiently occur throughout the full extent of the liquid cloud layer. The raindrops sediment at the downwind side of the hills that trigger the orographic cloud formation. Drops created too far in the lee are evaporated. This effect is mainly responsible for dampening the rain enhancement, as also observed in Siler and Roe (2014). In a warmer atmosphere, melting happens earlier such that accretion below is enhanced not only due to the overall increase in LWC but also because more melted hydrometeors fall through the liquid cloud layer. Therefore, although total melting is reduced, the mixed-phase seeder–

**Table 1.** Temperature sensitivity  $\alpha_P$  (in  $\% \text{ K}^{-1}$ ) of 24 h rainfall  $P$  for all  $n_{\text{CCN}}$  values.

$n_{\text{CCN}}$ ( $\text{cm}^{-3}$ )	$\Delta\Theta_v = -3 \text{ K}$	$\Delta\Theta_v = -1 \text{ K}$	$\Delta\Theta_v = +1 \text{ K}$	$\Delta\Theta_v = +3 \text{ K}$
50	0.76	0.50	1.01	1.40
200	1.35	1.06	1.17	1.41
500	1.79	1.53	1.40	1.17
800	2.03	1.80	1.69	1.19
1500	2.40	2.24	2.22	1.48

feeder effect leads to a strong enhancement of rainfall at locations close to the mountain ridge. However, the surface rain total increases less than the total water vapour inflow, mainly due to the decrease in the condensation ratio and enhanced evaporation.

Siler and Roe (2014) showed that the higher increase in condensation at high altitudes leads to a downwind shift of rainfall. This shift dominated in their idealized study and was not counteracted by the microphysical effect of the increased frozen-to-liquid hydrometeor ratio in a warmer atmosphere that can lead to an upwind shift in the distribution of precipitation. In this study, the faster processing of droplets indeed leads to an upwind shift in the rainfall pattern. A reason for the diverging results may be that in Siler and Roe (2014) most of the orographic rainfall sedimented on the upwind facing side of the mountain, due to lower wind speeds. Furthermore, Siler and Roe (2014) used an idealized terrain structure with solely one peak, while the terrain in the Lake District is more complex. In this study, the rainfall is deposited on the lee slopes of the peaks. In addition to faster processing, the rainwater solely produced by melting is evaporated over the valley in the warming scenario.

In terms of total precipitation, Siler and Roe (2014) found an increase in  $P$  of  $4.7 \% \text{ K}^{-1}$  and Sandvik et al. (2018) found an increase of  $5 \% \text{ K}^{-1}$ , while in this study the 24 h rainfall increase varies between  $0.5 \% \text{ K}^{-1}$  and  $2.4 \% \text{ K}^{-1}$  depending on the temperature perturbation and CCN concentration. This discrepancy in  $\alpha_P$  may be due to the choice of the integration domain as discussed in Sect. 3.1 and due to the lower temperature sensitivity of  $I$  in this study compared to others. The surface temperature range in Siler and Roe (2014) and Sandvik et al. (2018) is comparable to this study (i.e.  $T_{\text{surface}} \approx 10\text{--}15 \text{ }^\circ\text{C}$ ). Comparable with the  $6.0 \% \text{ K}^{-1}$  increase in  $P$  above 600 m a.s.l. found in this study, Sandvik et al. (2018) found a stronger increase in precipitation at high altitudes. Above 650 m a.s.l.  $P$  increases by  $6.4 \% \text{ K}^{-1}$  and below 150 m a.s.l.  $P$  increases by  $2.3 \% \text{ K}^{-1}$  (Sandvik et al., 2018). However, in this study the amount of rainfall decreases at altitudes below 150 m. An intensification of heavy orographic rainfall (sedimenting at high altitudes) at the expense of moderate and weak rainfall (sedimenting at low altitudes) is also found in an ensemble study over Norway that used a regional climate model to simulate a future climate

scenario (Poujol et al., 2021). Furthermore, a similar shift in the spatial distribution of precipitation but related to an increase in CCN and enhanced condensation was found by Alizadeh-Choozari (2018). A similarity between these effects is that precipitation was found to increase most in regions where the conversion of inflowing water vapour to rain is most efficient.

The temperature sensitivities of the condensation and drying ratios agree qualitatively with previous studies, although the magnitudes differ. In agreement with Sandvik et al. (2018), who found that CR decreases by  $3 \% \text{ K}^{-1}$ , the  $\alpha_{\text{CR}} = -3.4 \% \text{ K}^{-1}$  sensitivity found in this work dominates the sensitivity of DR. Besides the fact that moist air needs to be lifted higher up to reach saturation in a warmer atmosphere, the reduction in CR is mainly caused by the  $7.7 \% \text{ K}^{-1}$  reduction in frozen hydrometeor content. The total condensation  $C$  increases by  $5.4 \% \text{ K}^{-1}$  in the PB-plus3-500 scenario, comparable to the results obtained in the idealized study by Siler and Roe (2014), who found an increase in upstream condensation of  $5.7 \% \text{ K}^{-1}$ . Together with the slight reduction in PE, caused by the transition from cold-rain to less efficient warm-rain production and enhanced rain evaporation, the negative sensitivity of CR yields a total decrease in DR of  $\alpha_{\text{DR}} = -4.97 \% \text{ K}^{-1}$ . In fact, all studies discussed here find that DR decreases with temperature, mainly caused by the thermodynamic effect. Sandvik et al. (2018) found DR to decrease by  $1.2 \% \text{ K}^{-1}$  and Kirshbaum and Smith (2008) found  $\alpha_{\text{DR}} = -3.1 \% \text{ K}^{-1}$ . Presumably, those values are less extreme than the value obtained here of  $-4.97 \% \text{ K}^{-1}$  because the water vapour inflow in their simulations increased by  $10 \% \text{ K}^{-1}$  (Siler and Roe, 2014) and  $11 \% \text{ K}^{-1}$  (Kirshbaum and Smith, 2008), whereas in this study it is only  $\alpha_I = 5.88 \% \text{ K}^{-1}$ , which is partially explained by the smaller change in actual temperature compared to the  $\Delta\Theta_v$  offset. Other possible reasons for different  $\alpha_{\text{DR}}$  values are mountain width and horizontal wind speed. Eidhammer et al. (2018) found that the decrease in  $\alpha_{\text{DR}}$  is stronger for wider mountains because the microphysical timescale is larger. Furthermore, in the case of narrow mountains (width less than 50 km), the decrease in  $\alpha_{\text{DR}}$  is lower for lower horizontal wind speed. In fact, although absolute  $\alpha_{\text{DR}}$  is lower in Kirshbaum and Smith (2008), the half width in their experiment is more than 3 times bigger than in this study. Horizontal wind

speed in Kirshbaum and Smith (2008) and Siler and Roe (2014) is comparable to this study. Moreover, Siler and Roe (2014) found little dependence of  $\alpha_{\text{DR}}$  on horizontal wind speed.

Strong changes in CCN can modify the surface rainfall to a similar amount as the considered temperature changes. In our setup with fixed dynamics, these changes are approximately linearly independent of the temperature changes of thermodynamic and microphysical processes. At high CCN, the temperature sensitivity of surface precipitation is slightly higher than at low CCN concentrations but still small compared to CC scaling.

Despite the differences in numbers, the tendencies found in this study agree well with previous work on orographic precipitation under climate change. Total precipitation per event is expected to increase with temperature but at a lower rate than atmospheric water vapour. However, the mixed-phase seeder–feeder effect acts to focus the rainfall onto the highest elevations and thus poses great risk for flooding in and around mountainous regions.

## 5.2 Limitations and potential solutions

The piggybacking approach used to conduct this sensitivity study proves powerful to test microphysical sensitivities in isolation. However, locking the atmospheric dynamics excludes a big part of physics that itself is affected by climate change. Changes in global circulation patterns can affect the size, pathway and intensity of atmospheric rivers and mid-latitude cyclones. These large-scale changes in the location, frequency or dynamics of mid-latitude storms might be more important than local changes around certain mountain ranges (Siler and Roe, 2014; Shi and Durran, 2014). One approach to account for that problem could be to adjust  $\Delta\Theta_{\text{v}}$  not to be a constant offset but to be a three-dimensional field based on the output of a regional climate model, similarly to in Poujol et al. (2021). This way, more realistic temperature perturbations could be applied, although the dynamics remain identical. Eidhammer et al. (2018) used the pseudo-global-warming technique to simulate a future climate scenario. Their method also keeps the large-scale dynamics unchanged but allows vertical velocities to be adjusted.

Previous studies did not use piggybacking, and thus the comparison must be treated with care. However, those used for comparison here found low sensitivities of precipitation to changes in atmospheric dynamics (Sandvik et al., 2018; Siler and Roe, 2014; Kirshbaum and Smith, 2008).

Another limitation is the focus on a single case. This study thus lacks the more robust conclusions that could be derived from a larger statistical ensemble of various orographic rainfall events. As previously mentioned, the results depend strongly on the choice of the time period and evaluation domain. This is a general issue of single realistic studies, but it seems to be particularly challenging in the Cumbria case, due to its long duration and complex terrain. In order to general-

ize the findings, this study could be challenged by (a) performing further analyses of other extreme events in the same area, (b) splitting up the integration domain and the time interval and comparing the sensitivities obtained from each sub-domain, and (c) extending the analysis to other cases of extreme orographic precipitation. In general, coastal mountain ranges located at the west coast of continents, such as the Olympic Mountains in Washington (USA), the Norwegian coastal mountains or the Aoraki / Mount Cook National Park in New Zealand, are suitable choices if the synoptic conditions – air temperature, wind speed and direction, static stability – and the mountain geometry are comparable. A comparison of extreme precipitation events in cases with and without mixed-phase clouds could reveal the importance of melting as well as the potential for rain enhancement in a liquid-only cloud setting. A sensitivity analysis focusing on the mountain geometry, e.g. rescaling the orography as in Kirshbaum and Smith (2008) and Eidhammer et al. (2018), could help to generalize the findings.

## 6 Summary

This work analysed the temperature and CCN sensitivities of orographic rainfall embedded in a wintertime mid-latitude storm. To the authors' knowledge, it is the first study to apply piggybacking in sensitivity experiments of orographic rainfall.

A slight enhancement of  $1.6\% \text{ K}^{-1}$  of 24 h rainfall was found in the simulations with perturbed  $\Theta_{\text{v}}$ . The strong deviation from the  $7\% \text{ K}^{-1}$  CC scaling is due to the negative temperature sensitivity of the drying ratio. However, a  $6.0\% \text{ K}^{-1}$  increase in rainfall at the mountain peaks was found, whereas rainfall at low altitudes decreased by  $1.1\% \text{ K}^{-1}$ . The intensification of rainfall around the mountain peaks was caused by strongly enhanced accretion in a warmer atmosphere together with the upwind shift of melting, such that both processes have an increased vertical overlap. This effect is termed the mixed-phase seeder–feeder mechanism.

Analysis of non-dimensional efficiency measures showed that less efficient condensation and deposition of cloud condensate ( $\alpha_{\text{CR}} = -3.4\% \text{ K}^{-1}$ ) in a warmer climate is mainly responsible for the fact that rainfall enhancement is much lower than the increase in water vapour inflow ( $\alpha_{\text{DR}} = \alpha_{\text{CR}} + \alpha_{\text{PE}} = -4.97\% \text{ K}^{-1}$ ). Enhanced lee side evaporation of rainwater yields a slight decrease in precipitation efficiency ( $\alpha_{\text{PE}} = -1.57\% \text{ K}^{-1}$ ).

Separating the temperature and CCN contributions to total increase in  $P_{X,Y}$  showed that the individual contributions are independent of each other. If our findings are transferable to similar cases, orographic rainfall is expected to increase in both warmer and cleaner environments. The precipitation increases are largest over the mountain peaks, where the precipitation totals are already the largest, by the mixed-phase seeder–feeder mechanism. This implies that severe rainfall in

mountainous regions via the seeder–feeder mechanism may increase in future.

### Appendix A: Scaling parameters for different temperature and CCN scenarios

In the following, temperature sensitivities of the most relevant quantities analysed in this study are shown analogously to Table 1. They are calculated as relative changes from the corresponding  $\Delta\Theta_v = 0$  K scenario for each value of  $n_{\text{CCN}}$ , normalized by the respective temperature perturbation, as a proxy for the temperature sensitivity  $\alpha_X$  in units of  $\% \text{ K}^{-1}$ . This way, each table contains 5 · 4 values.

**Table A1.** Temperature sensitivity (in  $\% \text{ K}^{-1}$ ) of average rainwater content RWC for all  $n_{\text{CCN}}$  values.

$n_{\text{CCN}}$ ( $\text{cm}^{-3}$ )	$\Delta\Theta_v = -3$ K	$\Delta\Theta_v = -1$ K	$\Delta\Theta_v = +1$ K	$\Delta\Theta_v = +3$ K
50	11.68	13.46	14.13	13.91
200	12.27	13.96	14.44	14.42
500	12.91	14.63	14.54	13.58
800	13.19	14.93	14.81	13.20
1500	13.38	15.03	15.11	12.93

**Table A2.** Temperature sensitivity (in  $\% \text{ K}^{-1}$ ) of accretion for all  $n_{\text{CCN}}$  values.

$n_{\text{CCN}}$ ( $\text{cm}^{-3}$ )	$\Delta\Theta_v = -3$ K	$\Delta\Theta_v = -1$ K	$\Delta\Theta_v = +1$ K	$\Delta\Theta_v = +3$ K
50	12.53	14.25	14.71	14.13
200	13.01	14.75	15.40	15.83
500	13.41	15.17	15.13	14.96
800	13.63	15.33	15.27	14.34
1500	13.90	15.55	15.60	13.74

**Table A3.** Temperature sensitivity (in  $\% \text{ K}^{-1}$ ) of melting for all  $n_{\text{CCN}}$  values.

$n_{\text{CCN}}$ ( $\text{cm}^{-3}$ )	$\Delta\Theta_v = -3$ K	$\Delta\Theta_v = -1$ K	$\Delta\Theta_v = +1$ K	$\Delta\Theta_v = +3$ K
50	-3.91	-6.18	-8.93	-9.00
200	-3.45	-4.85	-6.86	-7.81
500	-3.73	-5.11	-6.36	-7.22
800	-3.83	-5.38	-6.39	-7.07
1500	-3.63	-5.42	-6.77	-7.07

**Table A4.** Temperature sensitivity (in  $\% \text{ K}^{-1}$ ) of rain evaporation for all  $n_{\text{CCN}}$  values.

$n_{\text{CCN}}$ ( $\text{cm}^{-3}$ )	$\Delta\Theta_v = -3$ K	$\Delta\Theta_v = -1$ K	$\Delta\Theta_v = +1$ K	$\Delta\Theta_v = +3$ K
50	14.33	17.20	17.67	18.04
200	15.96	19.77	22.06	23.94
500	16.36	20.51	23.49	25.88
800	16.34	20.31	23.49	25.29
1500	16.06	19.72	22.92	23.18

**Table A5.** Temperature sensitivity (in  $\% \text{ K}^{-1}$ ) of total water vapour inflow  $I$  for all  $n_{\text{CCN}}$  values.

$n_{\text{CCN}}$ ( $\text{cm}^{-3}$ )	$\Delta\Theta_v = -3$ K	$\Delta\Theta_v = -1$ K	$\Delta\Theta_v = +1$ K	$\Delta\Theta_v = +3$ K
All	5.05	5.30	5.60	5.88

**Table A6.** Temperature sensitivity (in  $\% \text{ K}^{-1}$ ) of the condensation ratio CR for all  $n_{\text{CCN}}$  values.

$n_{\text{CCN}}$ ( $\text{cm}^{-3}$ )	$\Delta\Theta_v = -3$ K	$\Delta\Theta_v = -1$ K	$\Delta\Theta_v = +1$ K	$\Delta\Theta_v = +3$ K
50	-4.82	-4.36	-3.81	-3.45
200	-4.85	-4.39	-3.83	-3.44
500	-4.87	-4.41	-3.83	-3.39
800	-4.88	-4.44	-3.86	-3.38
1500	-4.89	-4.50	-3.92	-3.39

**Table A7.** Temperature sensitivity (in  $\% \text{ K}^{-1}$ ) of the precipitation efficiency PE for all  $n_{\text{CCN}}$  values.

$n_{\text{CCN}}$ ( $\text{cm}^{-3}$ )	$\Delta\Theta_v = -3$ K	$\Delta\Theta_v = -1$ K	$\Delta\Theta_v = +1$ K	$\Delta\Theta_v = +3$ K
50	-1.13	-1.73	-1.53	-1.32
200	-0.41	-1.08	-1.44	-1.44
500	+0.19	-0.44	-1.16	-1.76
800	+0.49	-0.10	-0.80	-1.79
1500	+0.95	+0.42	-0.21	-1.54

**Table A8.** Temperature sensitivity (in  $\% \text{ K}^{-1}$ ) of the drying ratio DR for all  $n_{\text{CCN}}$  values.

$n_{\text{CCN}}$ ( $\text{cm}^{-3}$ )	$\Delta\Theta_v = -3$ K	$\Delta\Theta_v = -1$ K	$\Delta\Theta_v = +1$ K	$\Delta\Theta_v = +3$ K
50	-6.12	-6.16	-5.28	-4.63
200	-5.32	-5.52	-5.22	-4.74
500	-4.65	-4.88	-4.95	-4.97
800	-4.31	-4.54	-4.63	-4.98
1500	-3.80	-4.06	-4.12	-4.78

**Code and data availability.** ICON model output (two-dimensional fields) and post-processing scripts are available for download (Thomas et al., 2023, <https://doi.org/10.5445/IR/1000154410>). The full three-dimensional model output fields are available upon request.

**Author contributions.** AB developed the piggybacking implementation for ICON. AB and JT performed the numerical simulations. JT conducted the analyses, and all co-authors contributed to the interpretation of the results. JT wrote the paper, with support from all co-authors.

**Competing interests.** The contact author has declared that none of the authors has any competing interests.

**Disclaimer.** Publisher's note: Copernicus Publications remains neutral with regard to jurisdictional claims in published maps and institutional affiliations.

**Acknowledgements.** This work was performed on the computational resource ForHLR II funded by the Ministry of Science, Research and the Arts of Baden-Württemberg and DFG.

**Financial support.** This research has been supported by the Deutsche Forschungsgemeinschaft (grant no. BA 6521/1-1 in SPP 2115 and subproject B1 in SFB 165) and the H2020 European Research Council (grant no. ERC 714062).

The article processing charges for this open-access publication were covered by the Karlsruhe Institute of Technology (KIT).

**Review statement.** This paper was edited by Hailong Wang and reviewed by Omid Alizadeh and three anonymous referees.

## References

- Alizadeh-Choobari, O.: Impact of aerosol number concentration on precipitation under different precipitation rates, *Meteorol. Appl.*, 25, 596–605, <https://doi.org/10.1002/met.1724>, 2018.
- Alizadeh-Choobari, O. and Gharaylou, M.: Aerosol impacts on radiative and microphysical properties of clouds and precipitation formation, *Atmos. Res.*, 185, 53–64, <https://doi.org/10.1016/j.atmosres.2016.10.021>, 2017.
- Allen, R. and Ingram, W.: Constraints on future changes in climate and the hydrologic cycle, *Nature*, 419, 224–232, <https://doi.org/10.1038/nature01092>, 2002.
- Bechtold, P., Köhler, M., Jung, T., Doblas-Reyes, F., Leutbecher, M., Rodwell, M. J., Vitart, F., and Balsamo, G.: Advances in simulating atmospheric variability with the ECMWF model: From synoptic to decadal time-scales, *Q. J. Roy. Meteor. Soc.*, 134, 1337–1351, <https://doi.org/10.1002/qj.289>, 2008.
- Bergeron, T.: On the low-level redistribution of atmospheric water caused by orography, *Proceedings of the international conference on cloud physics*, Tokyo and Sapporo-shi, Japan, 24 May–1 June 1965, 96–100, 1965.
- Browning, K., Pardoe, C., and Hill, F.: The nature of orographic rain at wintertime cold fronts, *Q. J. Roy. Meteor. Soc.*, 101, 333–352, <https://doi.org/10.1002/qj.49710142815>, 1975.
- Dipankar, A., Stevens, B., Heinze, R., Moseley, C., Zängl, G., Giorgetta, M., and Brdar, S.: Large eddy simulation using the general circulation model ICON, *J. Adv. Model. Earth Sy.*, 7, 963–986, <https://doi.org/10.1002/2015MS000431>, 2015.
- Douglas, C. K. M. and Glasspoole, J.: Meteorological conditions in heavy orographic rainfall in the British isles, *Q. J. Roy. Meteor. Soc.*, 73, 11–42, <https://doi.org/10.1002/qj.49707331503>, 1947.
- Eidhammer, T., Grubišić, V., Rasmussen, R., and Ikdea, K.: Winter precipitation efficiency of mountain ranges in the Colorado Rockies under climate change, *J. Geophys. Res.-Atmos.*, 123, 2573–2590, 2018.
- Garvert, M. F., Smull, B., and Mass, C.: Multiscale Mountain Waves Influencing a Major Orographic Precipitation Event, *J. Atmos. Sci.*, 64, 711–737, <https://doi.org/10.1175/jas3876.1>, 2007.
- Grabowski, W. W.: Extracting microphysical impacts in large-eddy simulations of shallow convection, *J. Atmos. Sci.*, 71, 4493–4499, <https://doi.org/10.1175/JAS-D-14-0231.1>, 2014.
- Hande, L. B., Engler, C., Hoose, C., and Tegen, I.: Parameterizing cloud condensation nuclei concentrations during HOPE, *Atmos. Chem. Phys.*, 16, 12059–12079, <https://doi.org/10.5194/acp-16-12059-2016>, 2016.
- Heinze, R., Dipankar, A., Henken, C. C., Moseley, C., Sourdeval, O., Trömel, S., Xie, X., Adamidis, P., Ament, F., Baars, H., Barthlott, C., Behrendt, A., Blahak, U., Bley, S., Brdar, S., Brueck, M., Crewell, S., Deneke, H., Di Girolamo, P., Evaristo, R., Fischer, J., Frank, C., Friederichs, P., Göcke, T., Gorges, K., Hande, L., Hanke, M., Hansen, A., Hege, H., Hoose, C., Jahns, T., Kalthoff, N., Klocke, D., Kneifel, S., Knippertz, P., Kuhn, A., van Laar, T., Macke, A., Maurer, V., Mayer, B., Meyer, C. I., Muppa, S. K., Neggers, R. A. J., Orlandi, E., Pantillon, F., Pospichal, B., Röber, N., Scheck, L., Seifert, A., Seifert, P., Senf, F., Siligam, P., Simmer, C., Steinke, S., Stevens, B., Wapler, K., Weniger, M., Wulfmeyer, V., Zängl, G., Zhang, D., and Quaas, J.: Large-eddy simulations over Germany using ICON: a comprehensive evaluation, *Q. J. Roy. Meteor. Soc.*, 143, 69–100, <https://doi.org/10.1002/qj.2947>, 2017.
- Held, I. M. and Soden, B. J.: Robust Responses of the Hydrological Cycle to Global Warming, *J. Climate*, 19, 5686–5699, <https://doi.org/10.1175/JCLI3990.1>, 2006.
- Houze Jr., R. A. J.: Orographic effects on precipitating clouds, *Rev. Geophys.*, 50, RG1001, <https://doi.org/10.1029/2011RG000365>, 2012.
- Khain, A. P.: Notes on state-of-the-art investigations of aerosol effects on precipitation: A critical review, *Environ. Res. Lett.*, 4, 015004, <https://doi.org/10.1088/1748-9326/4/1/015004>, 2009.
- Kirshbaum, D. J. and Smith, R. B.: Temperature and moist-stability effects on midlatitude orographic precipitation, *Q. J. Roy. Meteor. Soc.*, 134, 1183–1199, <https://doi.org/10.1002/qj.274>, 2008.
- Kunz, M. and Kottmeier, C.: Orographic enhancement of precipitation over low mountain ranges. Part I: Model Formulation and

- Idealized Simulations, *J. Appl. Meteorol. Clim.*, 45, 1025–1040, <https://doi.org/10.1175/JAM2389.1>, 2006a.
- Kunz, M. and Kottmeier, C.: Orographic enhancement of precipitation over low mountain ranges. Part II: simulations of heavy precipitation events over Southwest Germany, *J. Appl. Meteorol. Clim.*, 45, 1041–1055, <https://doi.org/10.1175/JAM2390.1>, 2006b.
- Lavers, D. A. and Villarini, G.: The contribution of atmospheric rivers to precipitation in Europe and the United States, *J. Hydrol.*, 522, 382–390, <https://doi.org/10.1016/j.jhydrol.2014.12.010>, 2015.
- Lavers, D. A., Pappenberger, F., Richardson, D. S., and Zsoter, E.: ECMWF Extreme Forecast Index for water vapor transport: A forecast tool for atmospheric rivers and extreme precipitation, *Geophys. Res. Lett.*, 43, 11852–11858, <https://doi.org/10.1002/2016gl071320>, 2016.
- Marsh, T., Kirby, C., Muchan, K., Barker, L., Henderson, E., and Hannaford, J.: The winter floods of 2015/2016 in the UK – a review, Tech. rep., Centre for Ecology & Hydrology, 3 pp., ISBN: 978-1-906698-61-4, 2016.
- Matthews, T., Murphy, C., McCarthy, G., Broderick, C., and Wilby, R. L.: Super Storm Desmond: a process-based assessment, *Environ. Res. Lett.*, 13, 014024, <https://doi.org/10.1088/1748-9326/aa98c8>, 2018.
- Mlawer, E. J., Taubman, S. J., Brown, P. D., Iacono, M. J., and Clough, S. A.: Radiative transfer for inhomogeneous atmospheres: RRTM, a validated correlated-k model for the longwave, *J. Geophys. Res.-Atmos.*, 102, 16663–16682, <https://doi.org/10.1029/97jd00237>, 1997.
- O’Gorman, P. A.: Precipitation extremes under climate change, *Current Climate Change Reports*, 1, 49–59, <https://doi.org/10.1007/s40641-015-0009-3>, 2015.
- Payne, A. E., Demory, M. E., Leung, L. R., Ramos, A. M., Shields, C. A., Rutz, J. J., Siler, N., Villarini, G., Hall, A., and Ralph, F. M.: Responses and impacts of atmospheric rivers to climate change, *Nature Reviews Earth & Environment*, 1, 143–157, <https://doi.org/10.1038/s43017-020-0030-5>, 2020.
- Pfahl, S., O’Gorman, P. A., and Fischer, E. M.: Understanding the regional pattern of projected future changes in extreme precipitation, *Nat. Clim. Change*, 7, 423–427, <https://doi.org/10.1038/nclimate3287>, 2017.
- Pörtner, H.-O., Roberts, D., Tignor, M., Poloczanska, E., Mintenbeck, K., Alegría, A., Craig, M., Langsdorf, S., Löschke, S., Möller, V., Okem, A., and Rama, B.: *Climate Change 2022: Impacts, Adaptation and Vulnerability. Contribution of Working Group II to the Sixth Assessment Report of the Intergovernmental Panel on Climate Change*, Cambridge University Press, Cambridge, UK and New York, NY, USA, 2022.
- Poujol, B., Mooney, P. A., and Sobolowski, S. P.: Physical processes driving intensification of future precipitation in the mid- to high latitudes, *Environ. Res. Lett.*, 16, 034051, <https://doi.org/10.1088/1748-9326/abdd5b>, 2021.
- Prill, F., Reinert, D., Rieger, D., and Zängl, G.: *ICON Tutorial – Working with the ICON Model*, Deutscher Wetterdienst, Offenbach, Tech. rep., [https://doi.org/10.5676/DWD\\_pub/nwv/icon\\_tutorial2022](https://doi.org/10.5676/DWD_pub/nwv/icon_tutorial2022), 2022.
- Reinert, D., Prill, F., Frank, H., Denhard, M., Baldauf, M., Schraff, C., Gebhardt, C., Marsigli, C., and Zängl, G.: *DWD Database Reference for the Global and Regional ICON and ICON-EPS Forecasting System, Version 2.2.0*, Deutscher Wetterdienst, Tech. rep., [https://www.dwd.de/DWD/forschung/nwv/fe/pub/icon\\_database\\_main.pdf](https://www.dwd.de/DWD/forschung/nwv/fe/pub/icon_database_main.pdf) (last access: 9 January 2023), 2022.
- Sandvik, M. I., Sorteberg, A., and Rasmussen, R.: Sensitivity of historical orographically enhanced extreme precipitation events to idealized temperature perturbations, *Clim. Dynam.*, 50, 143–157, <https://doi.org/10.1007/s00382-017-3593-1>, 2018.
- Seifert, A. and Beheng, K.: A two-moment cloud microphysics parameterization for mixed-phase clouds. Part 1: Model description, *Meteorol. Atmos. Phys.*, 92, 45–66, <https://doi.org/10.1007/s00703-005-0112-4>, 2006.
- Shi, X. and Durran, D. R.: The Response of Orographic Precipitation over Idealized Midlatitude Mountains Due to Global Increases in CO<sub>2</sub>, *J. Climate*, 27, 3938–3956, <https://doi.org/10.1175/JCLI-D-13-00460.1>, 2014.
- Siler, N. and Roe, G.: How will orographic precipitation respond to surface warming? An idealized thermodynamic perspective, *Geophys. Res. Lett.*, 41, 2606–2613, <https://doi.org/10.1002/2013GL059095>, 2014.
- Smith, R. B. and Evans, J. P.: Orographic Precipitation and Water Vapor Fractionation over the Southern Andes, *J. Hydrometeorol.*, 8, 3–19, <https://doi.org/10.1175/jhm555.1>, 2007.
- Smith, S. A., Vosper, S. B., and Field, P. R.: Sensitivity of orographic precipitation enhancement to horizontal resolution in the operational Met Office Weather forecasts, *Meteorol. Appl.*, 22, 14–24, <https://doi.org/10.1002/met.1352>, 2015.
- Stow, D., Bradley, S., and Gray, W.: A preliminary investigation of orographic rainfall enhancement over low hills near Auckland New Zealand, *J. Meteorol. Soc. Jpn.*, 69, 489–495, [https://doi.org/10.2151/jmsj1965.69.4\\_489](https://doi.org/10.2151/jmsj1965.69.4_489), 1991.
- Thomas, J., Barrett, A. I., and Hoose, C.: Research data for “Temperature and CCN sensitivity of orographic precipitation enhanced by a mixed-phase seeder-feeder mechanism: a case study for the 2015 Cumbria flood”, KITopen [data set], <https://doi.org/10.5445/IR/1000154410>, 2023.
- Thompson, G. and Eidhammer, T.: A study of aerosol impacts on clouds and precipitation development in a large winter cyclone, *J. Atmos. Sci.*, 71, 3636–3658, <https://doi.org/10.1175/JAS-D-13-0305.1>, 2014.
- Zängl, G., Reinert, D., Rípodas, P., and Baldauf, M.: The ICON (ICOsahedral Non-hydrostatic) modelling framework of DWD and MPI-M: Description of the non-hydrostatic dynamical core, *Q. J. Roy. Meteor. Soc.*, 141, 563–579, <https://doi.org/10.1002/qj.2378>, 2015.